GSICS Global Space-based Inter-Calibration System

Quarterly

doi: 10.25923/1yfk-a604

Vol. 15 No 4, 2022

Newsletter Winter 2022 Issue

Editor: Manik Bali,

CMA • CNES • ESA • EUMETSAT • IMD • ISRO • JAXA • JMA • KMA • NASA • NIST • NOAA • ROSCOSMOS . ROSHYDROMET • SITP • USGS • WMO

Synergistic benefits of intercomparison between simulated and measured radiances of imagers onboard geostationary satellites

By S. J. Lee and M.-H. Ahn (Ewha Womans University)

Observations from infrared channels of four geostationary (GEO) satellite imagers are inter-compared by utilizing the radiative transfer model (RTM) simulations with the input of two NWP models. The results highlight the synergistic benefits of using NWP + RTM methods for the inter-calibration of GEO satellites by revealing features specific to a particular instrument and also by indicating uncertainties in the RTM and the NWP models. The details are described in [1] and a brief review of some of the results are reported here.

Observations from the Advanced Meteorological Imager (AMI) on board the GEO-KOMPSAT-2A, the Advanced Himawari Imager (AHI) on the Himawari-8, the Advanced Baseline Imager (ABI) on the GOES-16 and SEVIRI flying with the Meteosat-11 are inter-compared using the NWP + RTM method [2]. To demonstrate synergistic benefits of using the method, analysis fields from two NWP models (the Unified Model (UM) employed at the Korea Meteorological Administration and the ERA5 were utilized and the model equivalents were prepared using the radiative transfer for TOVs (RTTOV) v.12.3 [3].

The statistics of observations minus simulations (O–A) were analyzed over the clear-sky ocean as a function of time, space, observation angles, and scene temperatures for August 2019.

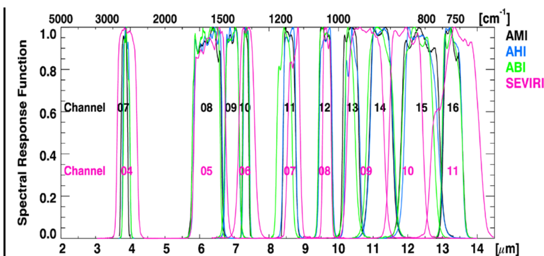

Figure Above shows SRFs of Ch 07–Ch 16 for AMI (black), AHI (blue), and ABI (green) and Ch 04–Ch 11 for SEVIRI (pink)

Overall O–A statistics (Table 1) show that there is no significant difference among the four imagers, displaying positive differences (in red color) in most of the water vapor channels and negative differences (in blue color) in the rest of the infrared channels. When compared to the GSICS results, the statistics for window channels (IR8~IR12) present slightly larger negative bias, and this is mostly attributed to residual clouds. Revisiting this issue with a stricter cloud detection scheme (conducted after the publication of [1]) provided much improved statistics, e.g., O–A for IR11 ranging from 0 to -0.05 K with respect to the ERA5. The results also show a couple of interesting features that need to be addressed.

First, both NWP models have positive bias with respect to the observations in the water vapor channels (except for ERA5 in WV3), confirming the wet bias in NWP model fields as was also found in the previous studies [4], [5]. In addition, the biases with

doi: 10.25923/1yfk-a604

GSICS Quarterly: Winter Issue 2022 **Volume 15, No. 4, 2022**

Channels			NWP model	Instrument			
AMI,AHI, ABI	SEVIRI	nicknames		AMI	AHI	ABI	SEVIRI
Ch07	Ch04	SW38	UM	-0.55 (0.66)	-0.97 (0.61)	-0.69 (0.67)	-0.08 (0.48)
			ERA5	-0.37 (0.53)	-0.75 (0.49)	-0.48 (0.55)	0.06 (0.40)
Ch08	Ch05	WV1	UM	0.58 (0.86)	0.35 (0.88)	0.43 (0.73)	0.67 (0.86)
			ERA5	0.38 (0.76)	0.16 (0.77)	0.23 (0.50)	0.34 (0.66)
Ch09		WV2	UM	0.44 (0.82)	0.47 (0.85)	0.48 (0.71)	
			ERA5	0.16 (0.71)	0.20 (0.73)	0.25 (0.48)	
Ch10	Ch06	WV3	UM	0.08 (0.68)	0.13 (0.69)	0.13 (0.55)	0.27 (0.65)
			ERA5	-0.21 (0.58)	-0.15 (0.58)	-0.11 (0.38)	-0.07 (0.50)
Ch11	Ch07	IR8	UM	-0.67 (0.49)	-0.65 (0.44)	-0.50 (0.33)	-0.63 (0.44)
			ERA5	-0.74 (0.45)	-0.70 (0.39)	-0.58 (0.29)	-0.70 (0.40)
Ch13		IR10	UM	-0.31 (0.42)	-0.34 (0.40)	-0.27 (0.32)	
			ERA5	-0.35 (0.35)	-0.38 (0.33)	-0.32 (0.27)	
Ch14	Ch09	IR11	UM	-0.22 (0.44)	-0.26 (0.43)	-0.15 (0.32)	-0.20 (0.41)
			ERA5	-0.34 (0.39)	-0.38 (0.37)	-0.27 (0.26)	-0.31 (0.35)
Ch15	Ch10	IR12	UM	-0.30 (0.47)	-0.49 (0.46)	-0.17 (0.33)	-0.34 (0.46)
			ERA5	-0.49 (0.42)	-0.68 (0.42)	-0.36 (0.28)	-0.58 (0.41)
Ch16	Ch11	CO2	UM	-0.17 (0.41)	0.05 (0.40)	-0.04 (0.27)	-0.06 (0.35)
			ERA5	-0.36 (0.39)	-0.14 (0.36)	-0.22 (0.23)	-0.33 (0.31)
# of matches			UM	1.7×107	2.1×107	1.7×107	1.5×107
			ERA5	4.4×106	5.4×106	7.1×106	3.9×106

Table1: Mean O–A (and standard deviation in parentheses) of AMI, AHI, ABI, and SEVIRI compared with the two NWP models for August, 2019 (unit: K).

respect to the UM are globally wetter compared to those from the ERA5. This feature can be also found in the spatial distribution of the biases of AMI, AHI, ABI, and SEVIRI for WV3 (Figure 1). The figure displays overall positive biases with the UM (top) and negative biases with the ERA5 (bottom), indicating the UM is more humid than the ERA5 in the mid-troposphere. Similar pattern was also found in WV1, the upper tropospheric water vapor channel [1].

Second, the spatial distribution of O–A for the CO_2 channels (Figure 2) reveal that a striping issue exists not only in AMI but also in AHI and ABI. Striping is clearly seen in the three advanced imagers regardless of the type of NWP models, while no stripes are found in SEVIRI. Usually, it is not easy to discern or identify such feature from one satellite imagery scene or from an O–A map for a short period of time, but the stripes become clearer when the analysis is done over sufficiently long period of time using NWP model data. The high spatial resolution of the imagers and NWP models is another contributor that enables the visualization of such a feature.

Lastly, there was an obvious satellite zenith angle dependence of O–A in IR8, whereas other infrared channels did not show such significant angle-dependency. Since the dependency appears not just in a specific instrument but in all instruments and with both

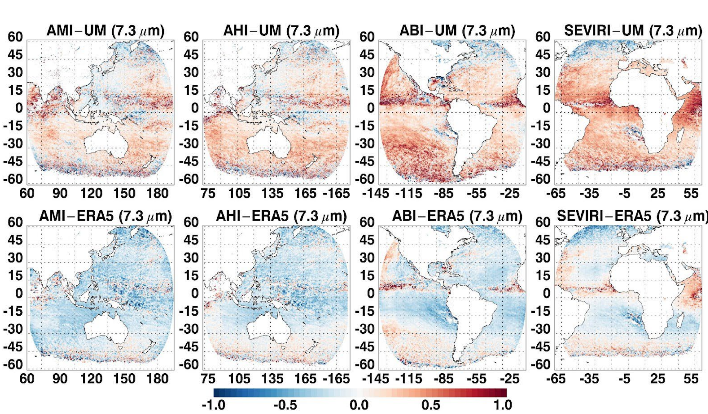

Figure 1. Spatial distributions of clear-sky O–A (unit: K) for AMI, AHI,

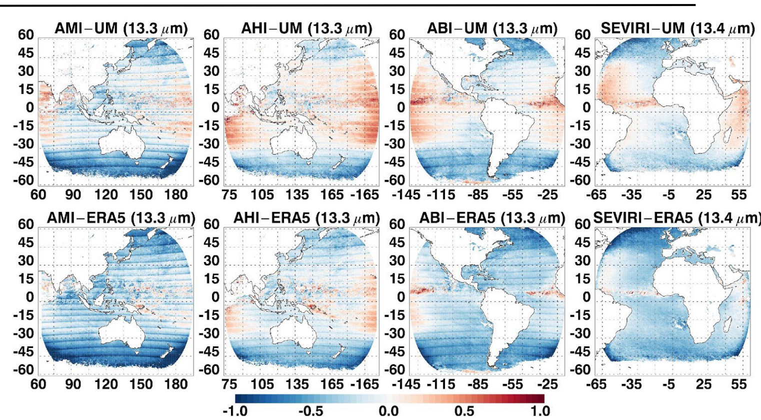

Figure 2. Same as in Figure 1 but for the channel of CO2.

doi: 10.25923/1yfk-a604

NWP models, the root cause is most in the sea surface emissivity model [6] Radiative Transfer Model (CRTM) by the authors, and it was found that the dependency decreases by up to 0.3 K at high zenith angles for AMI IR8 with the CRTM, suggesting the association of this issue with the RTM uncertainty.

References

[1] Lee, S. J. and Ahn, M.-H., 2021, Synergistic Benefits of Intercomparison Between Simulated and Measured Radiances of Imagers Onboard Geostationary Satellites. *IEEE Trans. Geosci. Remote Sens.*,Vol. 59, No. 12, 10725–37, 10.1109/TGRS.2021.3054030.

[2] Saunders, R. W., Blackmore, T. A., Candy, B., Francis, P. N., and Hewison,

likely RTM errors, particularly errors used in RTM. Further study was

T. J., 2013, Monitoring Satellite Radiance Biases Using NWP Models. *IEEE Trans. Geosci. Remote Sens.*, Vol. 51, No. 3, 1124–1138, 10.1109/TGRS.2012.2229283.

[3] Saunders, R., Hocking, J., Turner, E., et al., 2018, An update on the RTTOV fast radiative transfer model (currently at version 12). *Geosci. Model Dev.*, Vol. 11, 2717–2737, 10.5194/gmd-11-2717-2018.

[4] Xue, Y., Li, J., Li, Z., Lu, R., Gunshor, M. M., Moeller, S. L., Di, D., and Schmit, T. J., 2020, Assessment of Upper Tropospheric Water Vapor Monthly Variation in Reanalyses with Near-Global Homogenized 6.5 µm Radiances from Geostationary

conducted using the Community Satellites. *J. of Geophys. Res. Atmos.*, Vol. 125, No. 18, 10.1029/2020JD032695.

[5] Chung, E.-S., Soden, B. J., Sohn, B. J., and Schmetz, J., 2013, An assessment of the diurnal variation of upper tropospheric humidity in reanalysis data sets. *J. Geophys. Res. Atmos.*, Vol. 118, 3425–3430, 10.1002/jgrd.50345.

[6] Saunders, R., Hocking, J., Rundle, D., Rayer, P., Havemann, S., Matricardi, M., Geer, A., Lupu, C., Brunel, P., and Vidot, J., 2017, RTTOV-12 Science and Validation Report. EUMETSAT, NWPSAF-MO-TV-41.

Spectral Reflectance Estimation of UAS Multispectral Imagery Using Satellite Cross-Calibration Method

By Saket Gowravaram, Haiyang Chao, Andrew Molthan, Tiebiao Zhao, Pengzhi Tian, Harold Flanagan, Lori Schultz, and Jordan Bell (University of Kansas)

Introduction

Unmanned Aircraft Systems (UAS) are widely used for many multispectral remote sensing applications including disaster damage assessment [1,2], precision agriculture [3], and fire monitoring [4]. UAS can be programmed to fly autonomously at low altitudes under clouds and acquire multispectral images of a field at high spatial and temporal resolutions. However, one of the biggest challenges for UAS based multispectral remote sensing is the retrieval of reflectance from orthorectified UAS images in digital numbers (DN). Most existing UAS reflectance estimation techniques require reflectance target boards and spectroradiometers for each UAS survey mission which can be inconvenient and very expensive for a majority of UAS end users.

This article introduces a satellite-based cross-calibration (SCC) method for spectral reflectance estimation of UAS multispectral imagery. The SCC method provides a low-cost and feasible solution to convert high-resolution UAS images in DN to reflectance when satellite data is available. The main objective is to calibrate UAS DN images at high spatial resolution to reflectance using satellite surface reflectance (SR) data of the same area at lower spatial resolution as a reference. This method is demonstrated and validated by using a multispectral data set, including orthorectified KHawk UAS DN imagery and Landsat 8 Operational Land Imager Level-2 surface reflectance (SR) data over a forest/grassland area. The estimated UAS reflectance images are compared with National Ecological Observatory Network (NEON) Imaging Spectrometer SR data collected by a manned aircraft for validation. NEON is a continental-scale ecological observation facility project funded by NSF which covers 81 field sites across the USA annually. The proposed method will be beneficial to research groups who want to: (1) collect new UAS data but do not possess accurate spectroradiometers and ground target boards, (2) calibrate existing UAS data collected without a ground reflectance reference, and (3) study the radiometric relationships between multi-scale remote sensing data from satellite, manned aircraft, and UAS for enhanced

doi: 10.25923/1yfk-a604

earth observations. More details can be found in Gowravaram et al. (2021) [5].

Satellite-Based Cross-Calibration Method

Given an orthorectified UAS image X' in DN at high spatial resolution ($kM \times kN$ pixels) and a satellite atmospherically-corrected reflectance image Y at medium spatial resolution ($M \times N$ pixels), a cross-calibration function $F(X')$ can be identified for each spectral band that can convert UAS images in DN at high spatial resolution to spectral reflectance. Here, k is the ratio between the spatial resolutions of satellite and UAS images which can be derived from the data set. For example, k is 30 if the spatial resolutions of satellite and UAS images are 30 m and 1 m, respectively. The main steps of this method include:

1. UAS image resampling: Resample the high-resolution UAS image (X') to a medium-resolution image (X) to match the spatial resolution of the satellite image (Y). Existing methods like nearest neighbor, bilinear, or bicubic methods can be used. Bicubic interpolation is used in this work.
2. Pixel selection: Select UAS and satellite pixel pairs at medium spatial resolution, (X_1, Y_1), which is a subset of the original UAS and satellite image pair, (X, Y). Here, the objective is to exclude pixels that can potentially induce nontrivial errors in the function identification. High error pixels can be rejected using metrics such as sub-pixel coefficient of variation and shadow pixels as explained in detail in the section “Pixel Selection” in Gowravaram et al. (2021) [5].
3. Function identification: Use least-squares optimization methods to find the optimal cross-calibration function based on selected pixel pairs.
4. UAS reflectance estimation: Apply the identified function to the high-resolution UAS DN image (X') and finally obtain UAS reflectance image (Y').

Reflectance Estimation of KHawk UAS DN Images of Forest/Grassland Area in Kansas

The proposed SCC method is validated using a UAS and satellite multispectral data set, shown in Figure 1. It includes orthorectified high-resolution (1 m) KHawk DN and medium-resolution (30 m) OLI SR images all from the NIR band. For function identification, both Ordinary Least Squares (OLS) and Weight Least Squares (WLS) regression methods tested on the selected pixel pairs (Figure 1 right). The total error variance for NIR/red bands was 0.0061/0.0156 and 0.0011/0.0025 for the OLS and WLS methods, respectively. Therefore, the WLS method is selected for function identification.

Estimated KHawk Reflectance Validation Using NEON Imaging Spectrometer (NIS) Images

The estimated KHawk reflectance images at 1 m spatial resolution are compared to NEON Imaging Spectrometer (NIS) SR images at the same resolution for validation, shown in Fig. 2. It is worth mentioning that comparing all the pixels between the two images is difficult due to pixel alignment and georeferencing uncertainties. KHawk orthorectified images are generated from many images and has a RMSE error of 4.72 m. Six 3×3 m regions are manually selected for comparison, including three grass regions and three tree regions. The region size (3×3 m) is selected based on the average tree canopy size observed in this data set. Note that shadows are excluded from the selected regions for a fair comparison. The six NIS and KHawk reflectance values and differences between them are shown in Table 1.

Mean absolute error and RMSE were found to be 0.0243 and 0.0306 for the NIR band, and 0.0178 **a**nd 0.0163 for the red band.

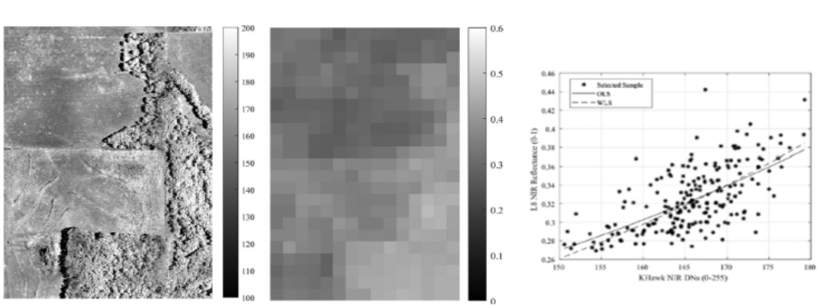

Figure 1. KHawk unmanned aircraft system and Operational Land Imager (OLI) near-infrared images of study area: orthorectified high-resolution KHawk digital numbers (DN) image (L), L8 OLI medium resolution SR (M), and KHawk DN vs L8 OLI SR scatter plot (R). UAS data was acquired 09:49–10:19 A.M. and L8 data was acquired 12:00 P.M. on June 7, 2017.

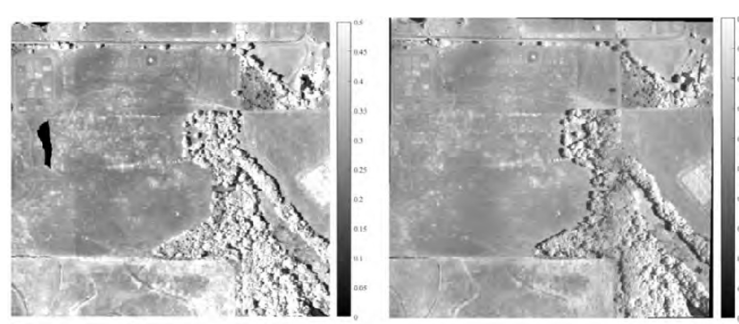

Figure 2. Calibrated NIS SR image (L) and estimated KHawk NIR SR image (R).

doi: 10.25923/1yfk-a604

Conclusions & Future Recommendations

In this article, a low-cost and novel SCC method is proposed for reflectance estimation of raw UAS DN images. This method only utilizes publicly available data without using ground calibration targets or expensive spectroradiometers, which makes it highly feasible for many UAS end users.

Future objectives include: (1) testing the effectiveness of the proposed method in other land cover; (2) development of ML-based algorithms for function identification; and (3) addressing the effects of spectral response difference in more detail; and (4) investigating the effect of BRDF correction on UAS reflectance estimation.

Reprinted with permission from the American Society for Photogrammetry & Remote Sensing, Bethesda, Maryland, asprs.org.

Table 1. Reflectance differences between NIS and KHawk

	NIR			Red		
Regions	NIS	KHawk	Difference	NIS	KHawk	Difference
Grass	0.2581	0.2595	0.0014	0.0577	0.0658	0.0082
Grass	0.2599	0.2736	0.0137	0.0487	0.0583	0.0096
Grass	0.2706	0.2787	0.0081	0.0501	0.0601	0.0100
Tree	0.4957	0.5454	0.0497	0.0343	0.0547	0.0204
Tree	0.5235	0.4762	0.0473	0.0224	0.0476	0.0251
Tree	0.4860	0.5118	0.0258	0.0229	0.0473	0.0244

References

[1] Wagner, Melissa, et al. "Unpiloted aerial systems (UASs) application for tornado damage surveys: Benefits and procedures." *Bulletin of the American Meteorological Society* 100.12 (2019): 2405-2409.

[2] Gowravaram, Saket, et al. "UAS-based multispectral remote sensing and NDVI calculation for post disaster assessment." *2018 International Conference on Unmanned Aircraft Systems (ICUAS)*. IEEE, 2018.

[3] Zhao, Tiebiao, et al. "A detailed field study of direct correlations between ground truth crop water stress and normalized difference vegetation index (NDVI) from small unmanned aerial system (sUAS)." *2015 International Conference on Unmanned Aircraft Systems (ICUAS)*. IEEE, 2015.

[4] Gowravaram, Saket, et al. "Prescribed Fire Monitoring Using KHawk Unmanned Aircraft Systems: Initial Flight Test Results." *2018 AIAA Information Systems-AIAA Infotech@ Aerospace*. 2018. 1491.

[5] Gowravaram, Saket, et al. "Spectral Reflectance Estimation of UAS Multispectral Imagery Using Satellite Cross-Calibration Method." *Photogrammetric Engineering & Remote Sensing* 87.10 (2021): 735-746.

Deconvolution of SNPP VIIRS solar diffuser bidirectional reflectance distribution function on-orbit change factor

By Ning Lei (Science Systems and Applications, Inc., Lanham, MD USA) and Xiaoxiong Xiong (NASA)

The Visible Infrared Imaging Radiometer Suite (VIIRS) is an Earth-observing satellite sensor [1]. Fourteen of the 22 VIIRS spectral bands are reflective solar bands (RSBs), covering wavelengths from 0.412 to 2.250 µm. The first VIIRS instrument is aboard the Suomi National Polar-orbiting Partnership (SNPP) satellite.

We calibrate the RSBs through an onboard solar diffuser (SD) with calibration data collected during the time when the SD is fully solar illuminated [2]. The change in the SD bidirectional reflectance distribution function (BRDF) value since launch, known as the H-factor, is determined by the SD stability monitor (SDSM). When in operation, the SDSM observes the Sun and the sunlit SD at almost the same time. The ratio of the SDSM detector signal strengths at the SD and the Sun views is a measure of the H-factor. The 8 SDSM detectors cover wavelengths from 0.412 to 0.926 µm.

Because the SDSM detector spectral response function spreads in wavelength, the directly measured H-factor, denoted by $H_{\mathrm{SDSM}}^{\mathrm{mea}}$, is the true H-factor, denoted by H_{SDSM}, convolved with the spectral response function [3]:

$$H_{\mathrm{SDSM}}^{\mathrm{mea}}\left(\lambda_d, t, \vec{\phi}(t)\right) = \frac{\int_0^{\infty} d\lambda \times \mathrm{SR}_{\mathrm{SDSM}}(\lambda,t,d)\Phi_{\mathrm{SUN}}(\lambda,t)H_{\mathrm{SDSM}}\left(\lambda,t,\vec{\phi}(t)\right)}{\int_0^{\infty} d\lambda \times \mathrm{SR}_{\mathrm{SDSM}}(\lambda,t,d)\Phi_{\mathrm{SUN}}(\lambda,t)}, \quad \ldots(1)$$

doi: 10.25923/1yfk-a604

where SR_{SDSM} denotes the SDSM detector spectral response function, λ_d is the detector center wavelength, t is time, $\vec{\phi}(t)$ is the solar angle at t, λ is the sunlight wavelength, d is the SDSM detector index, and Φ_{SUN} is the solar spectral power. $SR_{SDSM}(\lambda, t = 0, d)$ is derived from the prelaunch measurements.

To accurately deconvolve H^{mea}_{SDSM} to find H_{SDSM}, we have developed an iterative algorithm [4]. This algorithm depends on the fact that each SDSM detector response function has a main peak so that in Equation (1) the integral under the peak dominates. We separate the integral in the numerator in Equation (1) into the in-band (cutoffs at 1% of the peak value) and out-of-band parts and approximate the H_{SDSM} over the in-band wavelengths by $H_{SDSM}\left(\lambda_d, t, \vec{\phi}(t)\right)$ to arrive at

$$H^{mea}_{SDSM}\left(\lambda_d, t, \vec{\phi}(t)\right) = H_{SDSM}\left(\lambda_d, t, \vec{\phi}(t)\right)\int_{\text{in-band}} d\lambda \times SR'_{SDSM}(\lambda, t, d) + \int_{OOB} d\lambda \times SR'_{SDSM}(\lambda, t, d) \times H_{SDSM}\left(\lambda, t, \vec{\phi}(t)\right) \;...(2)$$

Where

$$SR'_{SDSM}(\lambda, t, d) = \frac{SR_{SDSM}(\lambda,t,d)\Phi_{SUN}(\lambda,t)}{\int_0^\infty d\lambda \times SR_{SDSM}(\lambda,t,d)\Phi_{SUN}(\lambda,t)} \;....(3)$$

We use the SDSM Sun view data to find $SR'_{SDSM}(\lambda, t, d)$ [3].
In the first iteration, we ignore the contribution from the out-of-band part to obtain

$$H_{SDSM}(\lambda_d, t, \vec{\phi}(t); 1\text{st}) = \frac{H^{mea}_{SDSM}(\lambda_d,t,\vec{\phi}(t))}{\int_{\text{in-band}} d\lambda \times SR'_{SDSM}(\lambda,t,d)}. \;.....(4)$$

For the nth iteration (n>=2),

$$H_{SDSM}(\lambda_d, t, \vec{\phi}(t); n\text{th}) = \frac{H^{mea}_{SDSM}(\lambda_d,t,\vec{\phi}(t)) - \int_{OOB} d\lambda \times SR'_{SDSM}(\lambda,t,d) \times H_{SDSM}(\lambda,t,\vec{\phi}(t);(n-1)\text{th})}{\int_{\text{in-band}} d\lambda \times SR'_{SDSM}(\lambda,t,d)} \;...\;(5)$$

We use a wavelength power law to

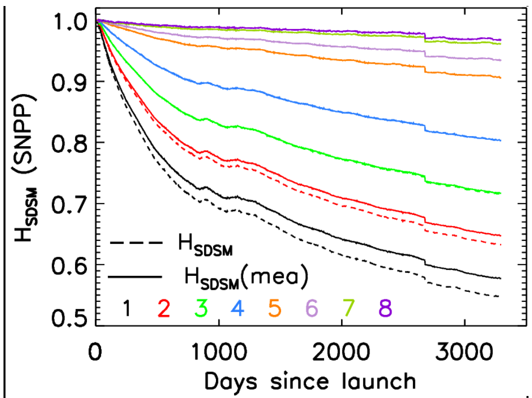

Figure 1. Measured (solid lines) and deconvolved (dashed lines) SNPP VIIRS SD H-factors at the SDSM SD view, versus time since the satellite launch. The SDSM detector indexes are shown in the figure.

extrapolate $H_{SDSM}(\lambda, t, \vec{\phi}(t); (n-1)\text{th})$ beyond the higher peak cutoff of the SDSM detector 8 [4]. We iterate the steps until the difference between the deconvolved H-factors in successive iterations is less than 0.0001. The number of iterations to reach the criterion is typically only 2 to 3.

Because within the spectral response function's main peak, we used, in the equations above, a constant across the wavelengths to approximate H_{SDSM}, we can improve the retrieval accuracy by removing the impact of the H-factor curvature in wavelength through adding

$$\text{deltaH} = \left(1 - \frac{\beta_H}{(\lambda_d/1\mu m)^{\eta_H}}\right) - \frac{\int_{\text{in-band}} d\lambda \times \left(1 - \frac{\beta_H}{(\lambda_d/1\mu m)^{\eta_H}}\right) \times SR'_{SDSM}(\lambda,t,d)}{\int_{\text{in-band}} d\lambda \times SR'_{SDSM}(\lambda,t,d)} \;....(6)$$

where β_H and η_H are obtained by fitting the H-factor wavelength power law to the originally retrieved values.

The deconvolved H-factors are nearly the same as the respective directly measured H-factors at the wavelengths equal to or longer than 0.488 µm (detector 3), as shown in Figure 1. But the deconvolved H-factors are significantly less than the respective measured H-factors at 0.412 µm (detector 1) and 0.445 µm (detector 2).

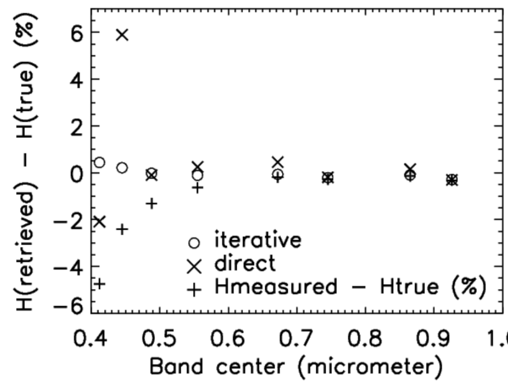

Figure 2. Difference in percentage between the retrieved and the hypothetical true H-factors using our iterative algorithm (circles) and the direct method (crosses) [4]. The pluses indicate the difference between the measured and the hypothetical true H-factors. The true H-factor is $1\text{-}0.0133/\lambda^4$ where λ is in micrometer. The detector spectral response function is Gaussian with the Gaussian width of 0.03 µm. The measurements contain a Gaussian noise having a Gaussian width of 0.25%.

These behaviors are due to the fact that the curvature of the H-factor versus wavelength curve becomes smaller toward longer wavelengths.

To illustrate the accuracy of the iterative deconvolution algorithm, we use a true function of $1\text{-}0.0133/\lambda^4$ where λ is in micrometer. The detector measurements contain Gaussian noises that have a width of 0.25% of the true signal. Eight detectors' spectral response functions are Gaussians with the same width of 0.03 µm. The respective peaks of the hypothetical detector response functions are at the respective design wavelengths of the VIIRS SDSM detectors (0.412, 0.445, 0.488, 0.555, 0.672, 0.745, 0.865, and 0.926 µm). Overall, the iterative algorithm yields much more accurate results than the popular direct method [4], especially at the two shortest wavelengths where the curvatures are the largest, as shown in Figure 2. The direct method's results are significantly influenced by noise whereas the iterative algorithm's results are much more stable.

In addition to the accuracy and the

doi: 10.25923/1yfk-a604

noise impact differences between the two approaches, the direct method is also much less flexible. In the example shown in Figure 2, the direct method uses a linear interpolation / extrapolation. A quadratic interpolation makes the direct method much more complex and a wavelength power law extrapolation makes the direct method impossible.

The deconvolved H-factors for the SNPP VIIRS are used to find the H-factors for the telescope SD view [3] denoted by H_{RTA}, through the following [3]

$$H_{\mathrm{RTA}} = \frac{H_{\mathrm{SDSM}}\times[1+\alpha_{\mathrm{RTA}}(1-H_{\mathrm{SDSM}})]}{1+\alpha_{\mathrm{H}}(1-H_{\mathrm{SDSM}})\times(\varphi_H-\varphi_0)} \quad \ldots(7)$$

where φ_H is the solar azimuth angle in the SD coordinate system and φ_0 is a reference angle [3]. We find α_{RTA} by fitting the F-factors (1/gain) calculated with Equation (7) to the F-factors derived from lunar observations [3]. The M1 band detector F-factors thus calibrated differ by as large as 0.7% from the F-factors calibrated by using the directly measured H-factor to replace H_{SDSM} in Equation (7) and the lunar F-factors. For the other RSBs, the differences are less. We believe that the calibration results with the deconvolved H-factors are more accurate.

Our iterative deconvolution algorithm can also efficiently retrieve other underlying true values where the detector response functions have respective main peaks.

References:

[1] Murphy, R. P., *et. al.* (2006). The visible infrared imaging radiometer suite. *Earth Science Satellite Remote Sensing*, **1**, 199-223, Springer-Verlag: New York, USA.

[2] Fulbright, J., et. al. (2016). Suomi-NPP VIIRS Solar Diffuser Stability Monitor Performance. *IEEE Trans. Geosci. Remote Sens.*, **54**, 631-639; doi: 10.1109/TGRS.2015.2441558.

[3] Lei, N., *et. al.* (2020). SNPP VIIRS RSB on-orbit radiometric calibration algorithms Version 2.0 and the performances, part 1: the algorithms. *J. Appl. Remote Sens.*, **14**, art-ID: 047501; doi: 10.1117/1.JRS.14.047501.

[4] Lei, N and X. Xiong (2022). Deconvolution of SNPP VIIRS Solar Diffuser Bidirectional Reflectance Distribution Function On-orbit Change Factor. *IEEE Trans. Geosci. Remote Sens.*, **60**, art-ID: 1000909; doi: 10.1109/TGRS.2021.3092682.

Status of the SLIMED lunar model

By Hugh Kieffer, Celestial Reasonings

The basis for lunar calibration is that the Moon is well-aged and its spectral reflectance properties are static to about 10^{-8} per annum [1], orders of magnitude better than diffuse standards. Lunar calibration has become a common technique, currently used primarily for trending. The lunar spectral irradiance model being used in most cases is the ROLO model [2] based on observations from a surface observatory. Many irradiance observations of the Moon from space are now available and can contribute to a model of the Moon. SLIMED is a methodology the makes use of many sources to generate a model as close to the true Moon as possible with a minimum number of terms; i.e., continuous in all geometric dimensions and wavelength.

Although the core of the SLIMED model is lunar reflectance, the product is a lunar spectral irradiance at standard distances in

$$E_{\odot}(\lambda) = S_{\odot}(\lambda,t)\frac{\Omega}{\pi D} \bullet R_0(P_0,\lambda)\, \mathbf{L}(P,w)\, \mathbf{B}(P,w)$$

the form

where $S_0(\lambda, t)$ is the solar spectral irradiance at 1 AU, the Hybrid Solar Reference Spectrum [3] is used. Variations of both total and spectral solar irradiance are small but well known; they are optionally included at the fit and/or calibration stage. The fraction accounts for the Moon's

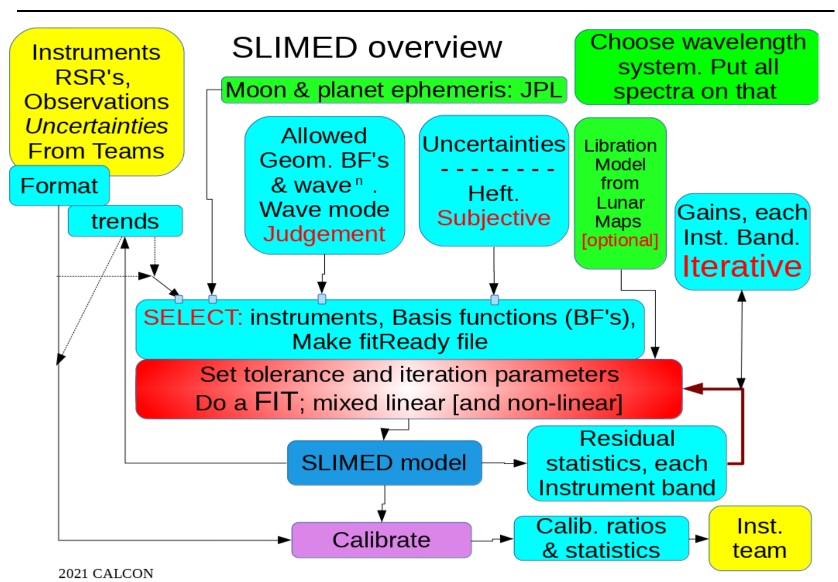

Figure 1: Simplified diagram of generation of a SLIMED model. Inside the red box are a few iterations unweighting statistical outliers. The loop represented by the red arrow is typically executed 15 times adjusting the empirical gains for each instrument band.

doi: 10.25923/1yfk-a604

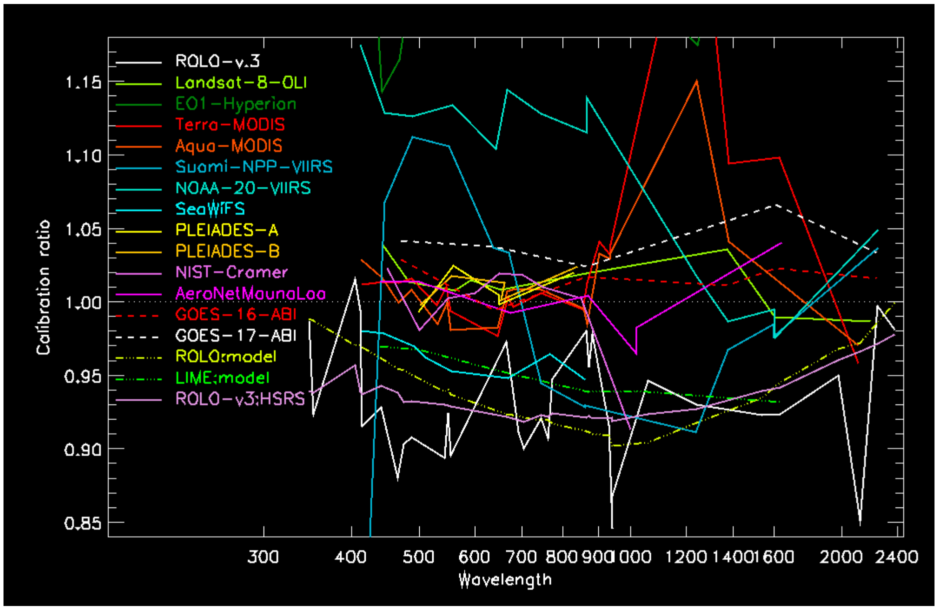

Figure 2: Calibration of several instruments (see color legend) using s SLIMED

size and distances to the Sun and viewer. The three terms after the dot make up the SLIM model of lunar disk-equivalent-reflectance: a function of wavelength and of five photographic angles represented by P, the same angles as used by ROLO [2]. $R_0(\lambda)$ is the high-resolution nominal Lunar reflection spectrum (LRS) based on laboratory measurementsof returned Apollo samples [4,5]; the 5% breccia mix used by [2] has been retained. **L** is a libration model based on global lunar maps of spectral reflectivity made from observations by spacecraft orbiting the Moon, 'MapLib'. These maps were made at photometric geometries quite different from the geometry of Earth-orbiting observations, but their global consistency should provide a good basis for estimating the effect of viewer direction on irradiance. B carries the variation of the lunar irradiance over angles and wavelengths as the sum of basis functions made up of the geometric angles and their product with polynomials of 'wave' w, which can be any of three modes: λ, $1/\lambda$ or $\ln \lambda$ with λ in μm. A general diagram of the SLIMED system is in Figure 1. The amount of data from instruments varies widely. To avoid an instrument dominating a SLIM model, a "heft" multiplies the weight of all data for an instrument to set its desired total weight. The SLIM system currently includes data submitted by teams for 24 instruments: Surface: ROLO [2], AeroNet Mauna Loa, NIST [6]; LEO: MODIS Terra and Aqua, Landsat-8 OLI, Hyperion, Suomi and NOAA-20 VIIRS, PLEIADES A and B; GEO: GOES 8:13 and 15 panchromatic, GOES 16 and 17 ABI,SEVIRI on MSG 1 to 4; Mars: HiRISE. Only surface and LEO are included in fits. Each instrument band is represented by its effective wavelength for the nominal lunar spectral irradiance. Broad bands ($\Delta\lambda/\lambda > 0.2$) are not included in fits but are in calibrations (these could also be represented by a few weighted effective wavelengths). A gain factor for each instrument band is adjusted as a model fit is iterated. The instruments in the SLIMED systems are simply those which were contributed, and hence somewhat arbitrary. Other teams are encouraged to submit observations. The SLIMED system is built to easily add instruments, which can improve the lunar model.

Generating a model involves many decisions, the model used here represents my best judgment; it includes MapLib, solar variation, and 34 geometric terms; the mean absolute weighted residual over 99,000 data points is 0.62%. The calibration results for GEO instruments are generally more noisy than LEO, and they have not been used in the model generation. All SLIMED models exhibit a drop in reflectance at the low and high wavelengths relative to the LRS, suggesting the need of an improved lunar reference spectrum. A manuscript describing the SLIMED system and its results has been submitted [7].

The band-average calibration results (reported irradiance divided by model irradiance, or gain bias) for all instruments that contributed to the model, plus the ABI's and two other lunar models, are shown in Figure 2. Eight instruments cluster below 880 nm, within about 3% of the SLIMED model; all but MODIS view the Moon directly. This is encouraging compared to the 5:7% uncertainty assigned to the ROLO model, which is 0:9% lower than SLIMED. SeaWiFS is about -5%. VIIRS and MODIS view the Moon with scan mirrors at different angles than nadir and show large differences; their calibration must be better than indicated by lunar calibration. Possible causes of large lunar calibration biases could be hardware related, e.g., thermal load

doi: 10.25923/1yfk-a604
GSICS Quarterly: Winter Issue 2022 Volume 15, No. 4, 2022

changes during attitude maneuvers between nadir and lunar look; or change in optics from a **Z-axis observation. Or they could be** due to the method of extracting lunar irradiance from a lunar observation. These large differences have been largely ignored in the past as lunar calibration has been primarily used for trending. The SLIMED system includes trending with a choice of five forms (combinations of linear and asymptotic) smoothed in time. Trends and an associated 'quality metric' have been derived for all bands of all instruments. Observations can be de-trended before inclusion in a fit; done only for Suomi-VIIRS in the model here. Sensitivity for determining trends is better than 0.1%; e.g., the scatter and annual oscillation seen in the SWIR bands of OLI using ROLO calibration are gone using this SLIMED model. Trends are large only for the early GOES instruments and the first VIIRS.

SLIMED has been developed in a proprietary language and the algorithm to generate a model needs to be converted to a generally-accessible form. The algorithm to use a model for calibration is much smaller; both algorithms access the JPL ephemeris. My hope is that more people will become involved, high-accuracy lunar observations on the horizon will prove out, the methods of extracting lunar irradiance from imaging will be refined, and thus the accuracy and precision of lunar calibration will improve.

References

[1] Kieffer, H.H., 1997. Photometric stability of the lunar surface, Icarus, 130,323–327

[2] Kieffer, H.H and T.C. Stone, 2005. The spectral irradiance of the Moon, Astron. Jour., 129:2887–2901

[3] Coddington, O.M., E.C. Richard, D. Harber, P. Pilewskie, T.N. Woods, K. Chance, X. Liu, and K.

[4] Sun, 2021, The TSIS-1hybrid solar reference spectrum, Geophys. Res. Lett., 48:777–707

[5] Pieters, C.M. 1999. The Moon as a calibration standard enabled by lunar samples. *http://www.planetary.brown.edu/pds/AP62231.html*

[6] Taylor, L.A, C.M. Pieters, L.P. Keller, R.V. Morris, and D.S. McKay, 2001, Lunar mare soils: Space weathering and themajor effects of surface-correlated nanophase Fe. Journal of Geophysical Research: Planets, 106(E11):27985–27999

[7] C.E. Cramer, C.E., K.R. Lykke, J.T. Woodward, and A.W. Smith, 2013, Precise measurement of lunar spectral irradiance at visible wavelengths, J. Res. Nat. Inst. Standards and Tech., 118

[8] Kieffer, H.H, Multiple Instrument based Spectral Irradiance of the Moon, 2022, J. Ap. Remote Sensing, submitted Dec. 2021

.

Lunar Calibration for a Microsatellite Sensor based on SELENE/SP model

By Masataka Imai (Kyoto Sangyo University), Junichi Kurihara (Hokkaido University), and Toru Kouyama (National Institute of Advanced Industrial Science and Technology)

Earth observation by nano / microsatellites has been developing rapidly over the past decade. However, onboard calibration hardware (e.g., solar diffuser panels, calibration lamps), cannot be equipped on nano / microsatellites due to size limitations. Lunar calibration, which utilizes the Moon as a reference source, is a relatively new radiometric calibration method for optical sensors, and it can provide an alternative measure to onboard calibration for nano/microsatellites. The U.S.

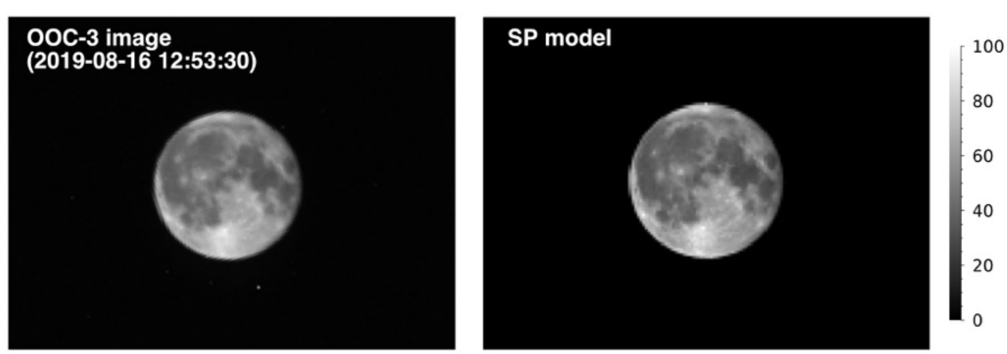

Figure 1. Moon images (165 × 124 pixels) captured by the OOC-3 (555 nm) band (left) and simulated by the SP model (right).

doi: 10.25923/1yfk-a604

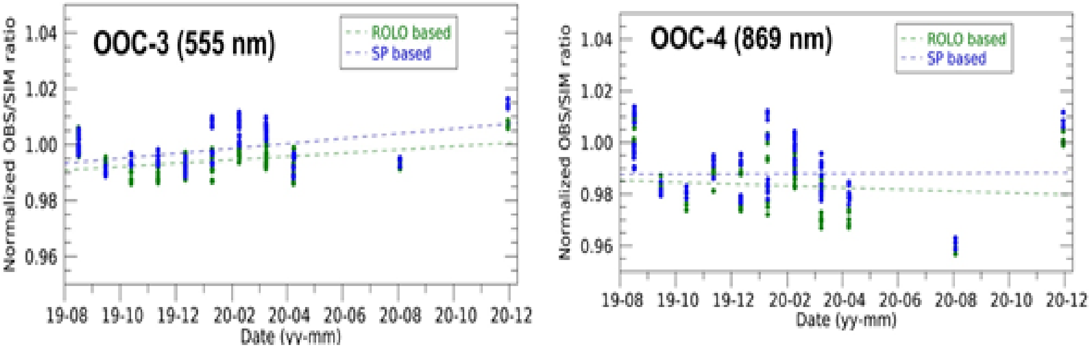

Figure 2. Temporal changes in the normalized observation-to-simulation irradiance ratio (OSR). The ROLO (green) and SP (blue) based OSR are shown in OOC-3 and -4 and dashed lines are linear regressions.

	OOC-3 (555 nm)		OOC-4 (869 nm)	
	ROLO	SP	ROLO	SP
Inclination (per year)	0.7%	1.1%	-0.4%	0.0%
Standard error	0.5%	0.7%	1.3%	1.3%

Table 1: Results of the linear regression analysis.

Geological Survey in Flagstaff established the ground-based RObotic Lunar Observatory (ROLO) and developed a Moon model (Kieffer and Stone, 2005), which can predict the irradiance of the Moon. While the precision of the ROLO model has been evaluated over a wide phase range in many studies (e.g. Stone, 2008), it has been pointed out the ROLO model has much larger discrepancies to other models (Keiffer, 2022). Although the ROLO model practically shows stable performance for evaluating relative values under the same phase angle condition, there could be a bias in absolute values. Thus, further inter-model comparisons are necessary for improving the accuracy of Moon models. Recently, another Moon model was developed using hyperspectral data obtained by the Spectrum Profiler (SP) onboard the SELENE Japanese Moon orbiter (Yokota et al., 2011; Kouyama et al., 2016). The SP model can reproduce the global brightness against any solar illumination and viewing condition for any Moon location (including the opposite side).

In this study, we applied lunar calibration to a multispectral sensor, Ocean Observation Camera (OOC), onboard a microsatellite named Rapid International Scientific Experiment Satellite (RISESAT) (Kuwahara et al., 2011). The OOC is a two-dimensional multispectral imager with four cameras (OOC-1: 405 nm /-2: 490 nm /-3: 555 nm /-4: 869 nm), whose bandwidths are approximately 10–20 nm. Moon observations by the OOC started on August 16, 2019, after seven months of the commissioning phase, and were continued until December 2020. The Moon surface brightness varies largely at a phase angle $|\alpha| \leq 7^{\circ}$ due to a strong backscattering or brightness opposition effect (Leach et al., 2019). Thus, Moon observations were carried out at an absolute phase angle of approximately 10° to obtain the maximum brightness, avoiding the backscattering surge.

The irradiance of the Moon at the satellite position at each observation time was simulated from both ROLO and SP models, and OOC sensitivity degradation was evaluated by calculating the observation-to-simulation irradiance ratio (OSR). The SP model simulates the lunar surface radiance at each grid specified by the solar incident angle (i), emission angle (e), and phase angle (α). The lunar surface radiance R_{SP} [W m^{-2} µm^{-1} sr^{-1}] is calculated as

$$R_{\mathrm{SP}}(\lambda) = r_{sim}(\lambda, i, e, \alpha)\frac{I_{\mathrm{Sun}}(\lambda)}{\pi}\left(\frac{1AU}{D}\right)^2$$

where r_{sim} is the radiance factor derived from the SP data, I_{Sun} is the solar irradiance [W m^{-2} µm^{-1}] at a distance of 1 [AU], and D represents the distance between the Sun and the Moon. It should be noted that the SP model covers 512.6−1600 nm whereas the ROLO model covers 350−2500 nm; thus, only OOC-3 and -4 were compatible with the SP model.

Figure 1 demonstrates the Moon radiance map from the SP model. Since the SP model has a resolution of 0.5° × 0.5° in lunar latitude and longitude (Kouyama et al., 2016), the SP model can provide a precise disk-resolved Moon radiance map. Therefore, even if an optical sensor's FOV is smaller than the full disk, the SP model can be utilized for the OSR calculation by addressing pixels in the observed image at high resolution.

The integrated Moon irradiance I [W m^{-2} µm^{-1}] over the disk both for observation and the SP model-simulated images were calculated as $I(\lambda) = \sum_j R_j(\lambda)\,\omega$, where the subscript j indicates the j-th pixel including the Moon disk region, R_j is the radiance, and ω is the instantaneous FOV of the pixels (as for OOC $(1.483\times10^{-4})^2$ [str]).

Figure 2 shows the temporal variations in the OSR normalized by the data obtained at the first month. While there were 0.5–1.3% of sensitivity variations in the standard error and >1% of

doi: 10.25923/1yfk-a604

deviation in each month, the estimated inclinations of the regression line were roughly within the range of 1% per year. Therefore, no significant sensor sensitivity degradation during the 16 months of the Moon observation period was confirmed (Table 1). The difference between the two models was < 1 %, and it was the same magnitude as Kouyama et al. (2017) achieved to measure relative sensor degradation on the order of 0.1% with the SP model. In conclusion, the SP model can provide an efficient radiometric calibration tool for a sensor onboard a microsatellite.

References:

Kieffer, H.H., and Stone, T.C., 2005, The Spectral Irradiance of the Moon. AJ 129, 2887–2901. https://doi.org/10.1086/430185

Kieffer, 2022. Status of the SLIMED lunar model, GSICS Quarterly Newsletter, DOI: 10.25923/1yfk-a604

Kouyama, T., et al., 2016, Development of an application scheme for the SELENE/SP lunar reflectance model for radiometric calibration of hyperspectral and multispectral sensors. Planetary and Space Science 124, 76–83. https://doi.org/10.1016/j.pss.2016.02.003

Kouyama, T., et al., 2017, Moon observations for small satellite radiometric calibration, in: 2017 IEEE International Geoscience and Remote Sensing Symposium (IGARSS). Presented at the 2017 IEEE International Geoscience and Remote Sensing Symposium (IGARSS), IEEE, Fort Worth, TX, pp. 3529–3532. https://doi.org/10.1109/IGARSS.2017.8127760

Kuwahara, T., et al., 2011, Satellite system integration based on Space Plug and Play Avionics, in: 2011 IEEE/SICE International Symposium on System Integration (SII). Presented at the 2011 IEEE/SICE International Symposium on System Integration (SII), pp. 896–901. https://doi.org/10.1109/SII.2011.6147568

Leach, N., Coops, N.C., and Obrknezev, N., 2019, Normalization method for multi-sensor high spatial and temporal resolution satellite imagery with radiometric inconsistencies. Computers and Electronics in Agriculture 164, 104893. https://doi.org/10.1016/j.compag.2019.104893

Stone, T.C., 2008, Radiometric calibration stability and inter-calibration of solar-band instruments in orbit using the moon, in: Earth Observing Systems XIII. Presented at the Earth Observing Systems XIII, International Society for Optics and Photonics, p. 70810X. https://doi.org/10.1117/12.795227

Yokota, Y., et al., 2011, Lunar photometric properties at wavelengths 0.5–1.6μm acquired by SELENE Spectral Profiler and their dependency on local albedo and latitudinal zones. Icarus 215, 639–660. https://doi.org/10.1016/j.icarus.2011.07.028

NEWS IN THIS QUARTER

GOES-T Launched

By Xiangqian (Fred) Wu, NOAA

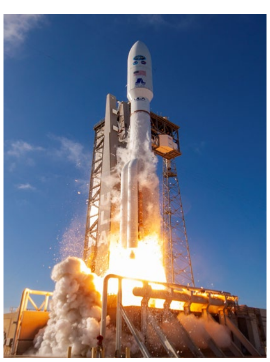

Geostationary Operational Environmental Satellite T (GOES-T) was launched at 16:38 EST on March 1, 2022, from Cape Canaveral, FL (Figure 1). It will be renamed as GOES-18 after reaching its orbit, and replace the ailing GOES-17 as GOES-WEST once commissioned. Extraordinary effort has been planned to make the Advanced Baseline Imager (ABI) date from GOES-18 available for NOAA operation before August 2022, which will be one of the most stressful time for GOES-17 ABI. These include accelerating the Post Launch Test (PLT) and Post Launch Product Test (PLPT), drifting away from the test site before completing all the tests, and delivering GOES-18 ABI data with GOES-17 data ("interleaving") before it is operational

doi: 10.25923/1yfk-a604

.

ACCURACy: Adaptive Calibration of CubeSat Radiometer Constellations

By John W. Bradburn and Mustafa Aksoy, Department of Electrical and Computer Engineering, University at Albany – State University of New York Albany, New York, USA

Introduction

Recent technological advances have enabled greater use of radiometer-equipped CubeSats for remote sensing missions. While CubeSats provide advantages with their low cost, weight, and power, there are notable drawbacks which pose challenges in radiometric calibration. A primary concern is that CubeSats may not have sufficient thermal mass or radiation shielding to ensure receiver stability at all times, resulting in an increased sensitivity to ambient conditions. This problem is exacerbated when power cycling the receiver, as may be sufficient to achieve stability under certain conditions but will also affect the time during which the radiometer may collect useful information. These issues result in compromises between stability and data collection. Another challenge with radiometer-equipped CubeSats is their ability to frequently calibrate, as due to the restrictions on cost, weight and size, it may not be possible to equip them with external blackbody calibration targets or internal references. To achieve a constellation-level absolute calibration it is then necessary to collect vicarious Earth calibration measurements, using radiative transfer models (RTMs), as well as cold space calibration measurements. To address these problems, ACCURACy uses instrument-level telemetry data to cluster constellation members into time-adaptive clusters of radiometers in similar states. By sharing calibration measurements between clustered radiometers, calibration data volume can be increased sufficiently to correct gain drifts and maintain low uncertainties in calibrated brightness temperature estimates.

ACCURACy Framework

ACCURACy is a framework consisting of three modules. The flow of data between these modules is depicted in Fig. 1. First, data is processed and clustered in the Clustering Module, which uses integrated telemetry data such as payload temperature measurements, age of instrument, and position to partition radiometers in a constellation into clusters. As radiometer gain and offset are typically determined by the physical temperature and age of the instrument, diometers which have similar temperature profiles and operational age may be considered to have similar gain and offset. This also must account for the hysteresis in the payload temperature of the instrument, and therefore in the radiometer gain, as the physical temperature will lag behind changes in ambient conditions due to saturation and other factors.

Second is the Calibration Pool module, which gathers calibration measurements and times corresponding to each cluster. For each cluster, calibration data is shared from each radiometer in that cluster with all other members of that

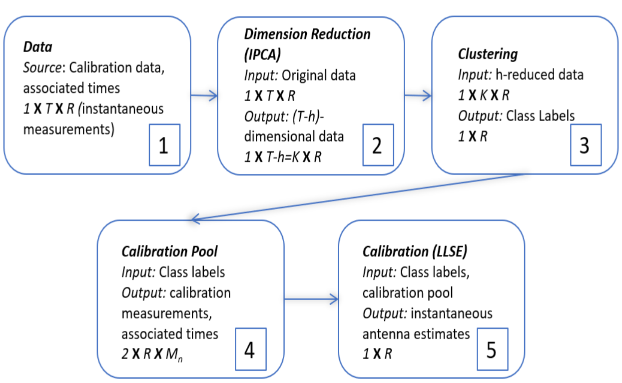

Figure 1. Data pipeline of ACCURACy, with data products shown at each step. Input calibration data and time are the raw input (1), which is preprocessed using PCA (2) before moving to the Clustering Module (3). Class labels associated with the cluster for each radiometer are used to form/update calibration pools (4), which are then used for calibrating each radiometer (5).

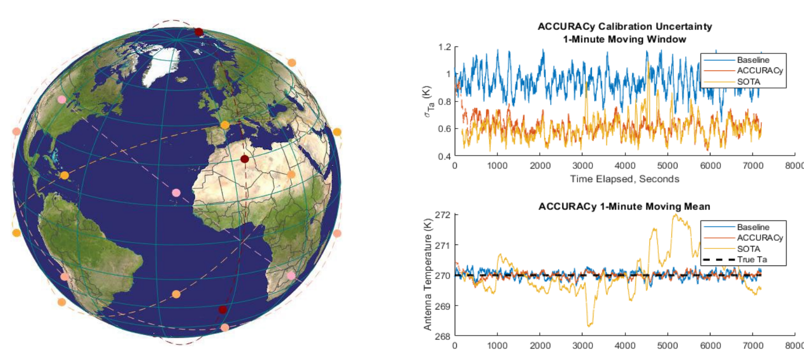

Figure 2. (**Left**) A simulation of 35 CubeSat radiometers orbiting the Earth. Some of the CubeSats are on polar orbits, and some are orbiting close to tropical regions near the equator. This is in part to ensure there are sufficient opportunities for CubeSats to overlap in the simulation. (**Top Right**) The calculated uncertainty (standard deviation) of the calibrated antenna temperature over 1-minute windows using the baseline, conventional SOTA, and ACCURACy methods. (**Bottom Right**) A moving mean of the calibrated antenna temperature calculated over a 1-minute window for the baseline, SOTA, and ACCURACy methods.

doi: 10.25923/1yfk-a604

same cluster. However, due to gain drift over time these accumulated calibration measurements may eventually produce errors when used to calibrate new cluster members, and so data will be only held in pools for a time interval determined by pre-launch laboratory data. This sub-module is able to detect error and uncertainty resulting from gain drift present in calibration measurements taken far apart and remove old calibration measurements or correct gain drifts.

Lastly, is the Calibration module, which uses data from calibration data pools to calibrate each radiometer in the constellation with calibration measurements respective to their cluster. An N≥2-point linear least squares calibration structure is created to estimate the gain and offset [1-2]. ACCURACy is also able to mathematically quantify the errors and uncertainties in calibration products, and establish measurement traceability, and assess calibration accuracy, sensitivity, and stability [2-4]. Large numbers of calibration measurements will lso help identify any calibration drifts and their impacts on the calibrated products, by calibrating one vicarious calibration reference target using theremaining calibration measurements.

Simulations and Initial Results

ACCURACy has been used with synthetic data to intercalibrate a constellation of simulated radiometers and obtain brightness temperature estimates for each constellation member. Fig. 2 shows a constellation of 35 simulated radiometers in orbit. The uncertainty and error in the estimated brightness temperatures of the simulated radiometers using ACCURACy perform better than the baseline, which is defined by calculating brightness temperature estimates for each radiometer using a 2-point LLSE every second with a one second resolution – as shown in Fig. 2.

Performance increase using ACCURACy can in part be attributed to averaging over a larger number of calibration data points. A conventional state-of-the-art (SOTA) intercalibration algorithm is also considered by calibrating multiple instruments using calibration measurements collected by them over approximately the same locations in orbit at approximately the same times [5-6]. This methodology is typically implemented as post-processing for current radiometer constellations. The approach employed by ACCURACy, on the other hand, results in lower error and uncertainty in calibrated brightness temperature estimates for a simulated radiometer constellation compared to both this approach and the baseline calculation. The resulting RMSE and variance for the calibrated antenna measurements using the baseline, SOTA, and ACCURACy methods are recorded in Table 1.

Algorithm	RMSE	σ^2
Baseline	0.93	0.87
ACCURACy	**0.62**	**0.38**
SOTA	0.83	0.68

Table 1. RMSE and Variance of brightness temperature estimates.

References

[1] P. Racette and R. H. Lang, "Radiometer design analysis based upon measurement uncertainty," Radio Science, vol. 40, no. 05, pp. 1–22,2005.

[2] M. Aksoy, H. Rajabi, P. E. Observations and Remote Sensing, vol. 13, p. 2807–2818, 2020.

[3] M. Aksoy and P. E. Racette, "A preliminary study of three-point onboard external calibration for tracking radiometric stability and accuracy," Remote Sensing, vol. 11, no. 23, p. 2790, 2019.

[4] M. Aksoy, P. E. Racette, and J. W. Bradburn, "Analysis of non-stationary radiometer gain via ensemble detection," in IGARSS 2019 - 2019 IEEE International Geoscience and Remote Sensing Symposium, 2019, pp.8893–8896.

[5] K. G. A. S.-G. W. L. J. S. K. Biswas, S. Farrar and S. Bilanow, "Intercalibration of microwave radiometer brightness temperatures for the global precipitation measurement mission," IEEE Transactions on Geoscience and Remote Sensing, pp. 1465–1477, 2013.

[6] T. Wilheit, W. Berg, H. Ebrahimi, R. Kroodsma, D. Mckague, V. Payne, and J. Wang, "Intercalibrating the GPM constellation using the gpm microwave imager (GMI),"2015 IEEE International Geoscience and Remote Sensing Symposium (IGARSS), p. 5162–5165, 2015.

doi: 10.25923/1yfk-a604

Announcements

Characterization and Radiometric Calibration for Remote Sensing (CALCON) annual meeting, September 12-15, 2022

By Stephanie Halton (SDL), Jim Butler and Xiaoxiong (Jack) Xiong (NASA)

The Characterization and Radiometric Calibration for Remote Sensing (CALCON) annual meeting will be held September 12-15, 2022 at Logan, Utah. CALCON provides a forum for scientists, engineers, and managers to present, discuss, and learn about calibration, characterization, and radiometric issues within the microwave, IR, visible, and UV spectral ranges. GSICS members are encouraged to attend the conference. Abstracts are due April 8, 2022. For more details, please visit http://www.calcon.sdl.usu.edu/.

GSICS-Related Publications

Boesch, H., et al. "SI-traceable space-based climate observation system: a CEOS and GSICS workshop, National Physical Laboratory, London, UK, 9-11 Sept 2019." (2022). http://doi.org/10.47120/npl.9319

Doelling, David R., Conor Haney, Rajendra Bhatt, Benjamin Scarino, and Arun Gopalan. 2022. 'Daily Monitoring Algorithms to Detect Geostationary Imager Visible Radiance Anomalies'. *Journal of Applied Remote Sensing* 16 (1): 1–18. https://doi.org/10.1117/1.JRS.16.014502

Galib, Mohd, Sutapa Bhattacharjee, and Rishikesh Bharti. 2022. 'Intercalibration of DMSP-OLS and NPP-VIIRS to Develop Enhanced Night-time Light Time-series for Evaluating the Urban Development Pattern of Major Indian Metropolitan cities'. https://doi.org/10.1002/essoar.10510603.1

J. Tian and J. Shi, "A high-accuracy and fast retrieval method of atmospheric parameters based on genetic-BP," in *IEEE Access*, doi: 10.1109/ACCESS.2022.3151868.

Lee, Su Jeong, and Myoung-Hwan Ahn. 2021. 'Synergistic Benefits of Intercomparison Between Simulated and Measured Radiances of Imagers Onboard Geostationary Satellites'. *IEEE TRANSACTIONS ON GEOSCIENCE AND REMOTE SENSING* 59 (12): 10725–37. https://doi.org/10.1109/TGRS.2021.3054030

Yang, W., H. Meng, R.R. Ferraro, and Y. Chen. 'Inter-Calibration of AMSU-A Window Channels'. *Remote Sensing* 12, no. 18 (2020). https://doi.org/10.3390/RS12182988.

Yu, F., X. Wu, H. Yoo, H. Qian, X. Shao, Z. Wang, and R. Iacovazzi. 2021. 'Radiometric Calibration Accuracy and Stability of GOES-16 ABI Infrared Radiance'. *Journal of Applied Remote Sensing* 15 (4). https://doi.org/10.1117/1.JRS.15.048504.

Submitting Articles to the GSICS Quarterly Newsletter:

The GSICS Quarterly Press Crew is looking for short articles (800 to 900 words with one or two key, simple illustrations), especially related to calibration / validation capabilities and how they have been used to positively impact weather and climate products. Unsolicited articles may be submitted for consideration anytime, and if accepted, will be published in the next available newsletter issue after approval / editing. Please send articles to manik.bali@noaa.gov.

doi: 10.25923/1yfk-a604

With Help from our friends:

The GSICS Quarterly Editor would like to thank Sri Harsha Madhavan (SSAI), Tim Hewison(EUMETSAT), Martin Burgdorf (University of Hamburg), David R. Doelling (NASA) and Lawrence Flynn (NOAA) for reviewing articles in this issue. Thanks are due to Jan Thomas (NOAA) for helping with 508 compliance.

Published By

GSICS Coordination Center
NOAA/NESDIS/STAR NOAA
Center for Weather and Climate Prediction,
5830 University Research Court
College Park, MD 20740, USA

CISESS
5825 University Research Court, Suite 4001,
University of Maryland, College Park, MD 20740-3823